DOI：10. 13471/j. cnki. acta. snus. 2022D010

Effect of sea salt aerosols on a warm-sector heavy rainfall event over coastal Southern China*

LUO Qing[1,2], *CHEN Zijian*[1,2], *LIN Wenshi*[1,2]✉, *JIANG Baolin*[3], *CAO Qimin*[1], *LI Fangzhou*[1]

1. School of Atmospheric Sciences / Guangdong Province Key Laboratory for Climate Change and Natural Disaster Studies, Sun Yat-sen University, Zhuhai 519082, China
2. Southern Marine Science and Engineering Guangdong Laboratory (Zhuhai), Zhuhai 519082, China
3. School of Geography and Tourism, Huizhou University, Huizhou 516007, China

Abstract: This study used the Weather Research and Forecasting model coupled with Chemistry (WRF-Chem) version 4.1.2 to simulate a warm-sector heavy rainfall (WSHR) event that occurred over coastal Southern China in 2014. To investigate the effects of the concentration of sea salt aerosols (SSA) on the development of WSHR, different levels of SSA emission were incorporated in three separate experiments (CTL, LOW, and HIGH). The distribution of precipitation and hydrometeors, the microphysical processes, and the release of latent heat resulting from the rainfall in all three simulations were analyzed. Results show that SSA mass concentration can affect the rainfall area: the LOW experiment shows dispersed rainfall, whereas the HIGH experiment presents concentrated rainfall. Under the situation of low (high) SSA emission: the concentration of cloud condensation nuclei during rainfall decreases (increases), the mixing ratio of rain and graupel increases (decreases), and microphysical processes, particularly the automatic conversion of cloud water into rainwater and accretion of cloud water by rain, are enhanced (weakened), more (less) latent heat is released, and the updrafts are enhanced (weakened); these result in an increase (decrease) of accumulated precipitation and rain rate.

Key words: sea salt aerosols; warm-sector heavy rainfall; microphysical effects; WRF-Chem model
CLC number: P401 **Document code:** A **Article ID:** 2097－0137（2023）02－0123－14

1 Introduction

Heavy rainfall that often occurs over Southern China (SC) during the first rainy season(April-June) can be one of the most devastating natural disasters. Warm-sector heavy rainfall (WSHR) is a special and important type of rainfall in SC that often causes severe flooding and huge economic losses. Generally, WSHR refers to precipitation that occurs in the warm zone approximately 200−300 km from the surface front, in the convergence zone between southwesterly and southeasterly flows, or in southwesterlies without a front and shear. Heavy rainfall in the warm region of SC, caused by microscale-mesoscale systems, usually happens abruptly and locally, making both objective forecasts and numerical model predictions difficult. On the one hand, such events are difficult to forecast owing to lack of synoptic-scale baroclinic system forcing such as fronts, shear, and vortices (Wu

* **Received**: 2022－02－27 **Accepted**: 2022－06－14 **Published online**: 2022－09－17
Supported by National Natural Science Foundation of China（41875168）

✉**Corresponding author**: LIN Wenshi（*linwenshi@mail.sysu.edu.cn*）

LUO Qing (*luoq57@mail2.sysu.edu.cn*), CHEN Zijian（*chenzj59@mail2.sysu.edu.cn*）,JIANG Baolin (*jiangblin@hzu.edu.cn*), CAO Qimin (*caoqm@mail2.sysu.edu.cn*), LI Fangzhou（*lifzhou@mail2.sysu.edu.cn*）

et al., 2020). For example, deterministic operational numerical weather prediction models failed to forecast the typical local warm-sector rainfall event that occurred over Guangzhou (China) on May 7, 2017 (Wu et al.,2018). On the other hand, when using a numerical model to simulate WSHR, one of the most critical factors is the capability of the cloud microphysical parameterization scheme to effectively describe the cloud microphysical processes (Gao et al., 2012). Therefore, employing a numerical model to simulate WSHR and using the results to analyze the mechanism of the cloud microphysical characteristics could improve the understanding of WSHR and provide scientific reference for improving the capability of numerical models to forecast such events.

Aerosols can act as cloud condensation nuclei (CCN) and participate in the formation of cloud droplets, thereby changing the concentration and size distribution of cloud droplets, and thus affecting hydrometeor distribution, cloud lifetime, and precipitation (Twomey, 2012; Rosenfeld 2008). Rosenfeld (1999; 2020) observed that aerosol concentration was increased by biomass combustion, which narrowed the cloud droplet spectrum and inhibited the collision process, leading to reduced precipitation. Lohmann et al. (2005) revealed that aerosols can act as ice-forming cores at high altitudes, thereby promoting deep convection and increasing surface precipitation. Other research used simulation results to demonstrate quantitatively that an increase in aerosol concentration could lead to a 23.4% decrease in topographic cloud precipitation (Xiao et al., 2014).

Sea salt aerosols (SSA) are one of the main aerosols in oceanic and coastal areas (Lewis et al., 2004). They are generated primarily from spume or emitted during bubble bursting at the sea surface (Monahan et al., 1986). As CCN, SSA can participate in cloud microphysical processes, chemical reactions, and the dry-wet sedimentation process (Gong et al., 1997). Previous studies focused on the transmission of atmospheric momentum and heat flux by oceanic droplets and the effect of SSA on typhoons. For example, Rosenfeld et al. (2002) found that aerosols generated by oceanic droplets were conducive to removing pollutants in the atmosphere and enhancing the process of collection of cloud droplets by raindrops. Herbener et al. (2014) proved that an increase in aerosol concentration in the cloud wall area would strengthen a typhoon, whereas an increase in aerosol concentration in the periphery of a typhoon would cause it to weaken. Jiang et al. (2019) and Luo et al. (2019) both studied the influence of SSA as CCN on the cloud microphysical processes, precipitation, and thermal processes of typhoon using numerical models, and they found that SSA can promote the transformation of cloud water and the process of its collection by raindrops, thereby increasing precipitation. However, it remains unclear how SSA-cloud interactions might influence heavy rainfall events.

Southwesterly winds can carry SSA to SC and affect local precipitation. On the basis of multisource observational data, Li et al. (2021) preliminarily discussed the influence of SSA on the microphysical processes and internal dynamics of the heavy rainfall event that occurred over SC on May 7, 2017. Additionally, Guo et al. (2022) explored the effects of anthropogenic aerosols and SSA on heavy rainfall in early summer (June 2019) over the monsoon coastal region of China. However, studies on the role of SSA regarding the intensity and microphysical processes of heavy rainfall in SC, especially in terms of WSHR, remain limited.

The objective of this study was to investigate the effects of SSA on WSHR over SC. For this purpose, a typical WSHR event that occurred over SC in May 2014 was selected and subsequently simulated using the Weather Research and Forecasting Model coupled with Chemistry (WRF-Chem) (Grell et al., 2005; Skamarock et al., 2008). The model setup and the experimental design are described in detail in Section 2. An overview of the WSHR event is provided in Section 3. Section 4 presents the results of the modeled precipitation and further reveals the effects of SSA on the heavy rainfall. Finally, the main conclusions are summarized in Section 5.

2 Model configuration and experimental design

The WRF-Chem model version 4.1.2 was used in this study to simulate meteorological fields coupled with gas-chemistry and aerosols. WRF-Chem is a non-hydrostatic fully compressible model in which the constitution and number concentration of aerosols are predicted explicitly. The simulation period started at 12:00 UTC on May 10, 2014 and ended at 00:00 UTC on May 12, 2014. The first 12 h were regarded as the spin-up time. The period from 00:00 UTC on May 11 to 00: 00 UTC on May 12, 2014 was used for the analysis. The model was configured with three domains: d01, d02, and d03 (Fig.1a). The outermost domain (d01) had horizontal grid resolution of 36 km, while domains d02 and d03 had horizontal grid resolution of 12 and 4 km, respectively. The key region of this study (21.5°−23.5°N, 113°−115°E) encompassed the area in which the selected WSHR event happened, it included the Pearl River Delta and some offshore areas. The key region is indicated by the gray dashed rectangle in Fig. 1b. The meteorological initial and boundary conditions were set using the NCEP FNL dataset (http://rda.ucar.edu/datasets/ds083.2) with 1°×1° spatial resolution and 6 h temporal resolution. To improve the simulation results in the boundary layer, 40 vertical levels were used from the surface up to 50 hPa at the model top.

The microphysical scheme used was that of Lin et al. (1983), which predicts cloud droplet number and size by determining aerosol activation in the WRF-Chem model (Liu et al., 2004). The Grell-3 cumulus parameterization scheme (Grell et al., 2002) was used in domains d01 and d02. No parameterization scheme for cumulus convection was employed in d03 because of the ability of the grids with 4 km resolution to clearly distinguish cloud-scale processes. The other major physical schemes used included the Rapid Radiative Transfer Model for Global Climate Models longwave and shortwave radiation schemes (Iacono et al., 2008), the unified Noah land surface model (Livneh et al., 2011), and the revised MM5 Monin-Obukhov surface-layer scheme (Jiménez et al., 2012).

The Model for Simulating Aerosol Interactions and Chemistry using eight sectional aerosol bins (Zaveri et al., 2008) provided simulations of gases and aerosols; the aerosols considered comprised sulfate, nitrate, sea salt, ammonium, organic carbon, black carbon, other inorganics(e. g., silica, other inert minerals, and trace metals), and liquid water. The Carbon-Bond Mechanism version Z (Zaveri et al., 1999) was adopted for gas-phase atmospheric chemistry. The Fast-J scheme (Wild et al., 2000; Barnard et al., 2004) was

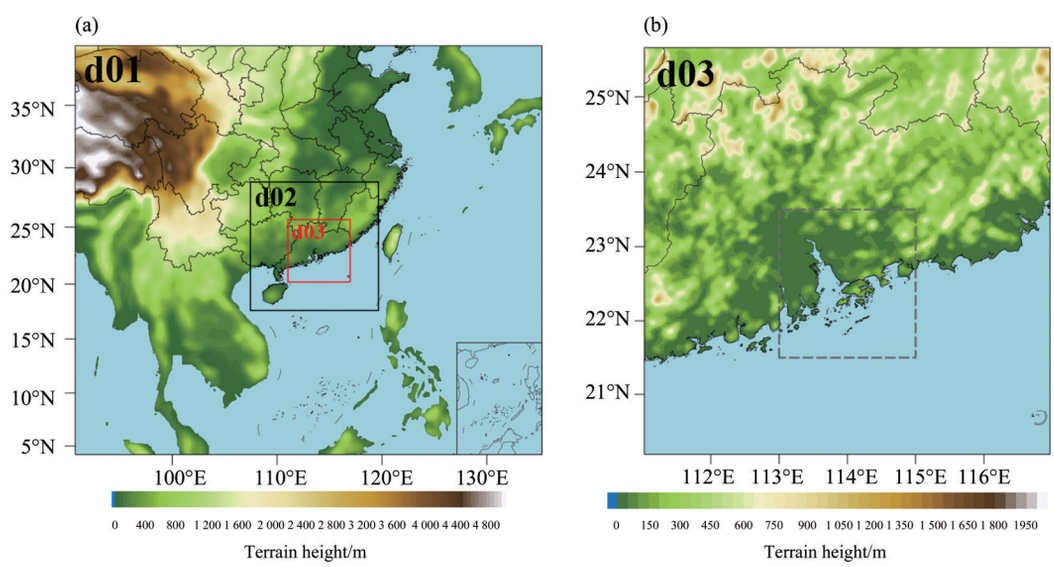

Fig. 1　(a) The three nested model domains with horizontal resolution of 36 km (d01), 12 km (d02), and 4 km (d03) with terrain height (shading; unit: m); (b) Domain d03 showing the key region of this study (21. 5°−23. 5°N, 113°−115°E) indicated by the gray dashed rectangle

used for photolytic reaction rates. Inventories of anthropogenic emissions were are obtained from the Multi-resolution Emission Inventory for China(http://www.meicmodel.org), released by Tsinghua University (Zhang et al., 2009), which has 0.25° grid resolution and covers anthropogenic emissions from power plants, transportation, industry, agriculture, and activities related to residential areas. Biogenic emissions were obtained from the Model of Emissions of Gases and Aerosols from Nature (Guenther et al., 2006). Biomass burning emissions were computed at horizontal resolution of 1 km^2 on the basis of the global daily fire emissions in 2014 using the Fire Inventory from NCAR (https://www.acom.ucar.edu/Data/fire/) (Wiedinmyer et al., 2011). The chemical lateral boundary and initial conditions were derived from the results of the Community Atmosphere Model with Chemistry (Lamarque et al., 2012), which is a component of the NCAR Community Earth System Model used for simulations of global tropospheric and stratospheric atmospheric composition.

In the WRF-Chem model, SSA are mainly composed of sodium chloride, and their formation is mainly related to the development of spray droplets that form from the breakup of waves caused by the continuous flow across the sea surface. Generally, SSA have a broad size distribution and they can impact cloud droplet number concentration and cloud condensation as CCN. Because SSA are hydrophilic and large, they can easily be removed from the atmosphere; thus, their average lifetime is approximately only 0.6 d (Chin et al., 2002). The emission intensity of SSA (N_p per m^2, per second and per μm, where is number of particles) is often considered a function of sea surface wind speed, and it can be parameterized as below following Gong et al. (Gong et al., 1997):

$$\mathrm{d}F/\mathrm{d}r = 1.373W_{10}^{3.14}r^{-A}\left(1 + 0.057r^{3.45}\right) \times 10^{1.19\exp(-B)}, \quad (1)$$

where $A = 4.7(1 + \Theta r)C$, $B = (0.433 - \log r)/0.433$, $C = -0.017r^{-1.44}$, W_{10} is sea surface wind speed, r is the SSA radius (integrated over the size range of 0.1−10 μm in the model), and Θ is a parameter to adjust for the shape of the submicron-size distribution(set to 30 in this study) (Gong et al., 2003).

To investigate the effects of SSA on warm-sector rainfall, we designed three simulation experiments. The SSA emission in the control (CTL) experiment followed Eq. (1). In the two sensitivity experiments: LOW and HIGH, the coefficient of the sea salt aerosol flux emission was multiplied by 0.1 and 10, respectively. All other model settings were the same in each of the three simulations.

3 Case overview

A gridded dataset (resolution: 0.1° ×0.1°) of hourly precipitation was used to examine the spatiotemporal distribution of rainfall. After quality control, the dataset comprised 30 000−40 000 rain gauge observations from China and data from the U.S. Climate Precipitation Center Morphing (CMORPH) satellite retrieval precipitation products with 30 min temporal resolution and 8 km horizontal spatial resolution (http://data.cma.cn/).

A heavy rainfall event with more than 200 mm/d occurred in the coastal area of SC on May 10−12, 2014 (Luo et al., 2017). The observed 24 h rainfall accumulation from 00: 00 UTC on May 11 to 00: 00 UTC on May 12, 2014, exhibited two areas of heavy rainfall (>50 mm) inland and along the coastline, with the maximum rainfall amount exceeding 225 mm near Shenzhen. The area of inland rainfall was closely related to a northeast-southwest-oriented shear line at 850 hPa and a 500 hPa trough located north of the shear line (Fig. 2a-c). Guangdong is situated a few hundred kilometers to the south of the low-level shear line that was controlled by warm southwesterly winds at 850 hPa. As shown in Fig. 2d-f, precipitable water increased near the south coastal area because the shear line moved southward and the trough at 500 hPa became deeper. The area of coastal heavy rainfall was located on the leading edge of the boundary layer(BL) jet (Chen et al., 2018), which was over the northern region of the South China Sea and associated with a low-level vortex at 925 hPa over southwestern China. The strong southwesterly BL jet brought abundant moisture over the coastal area. Surface analysis

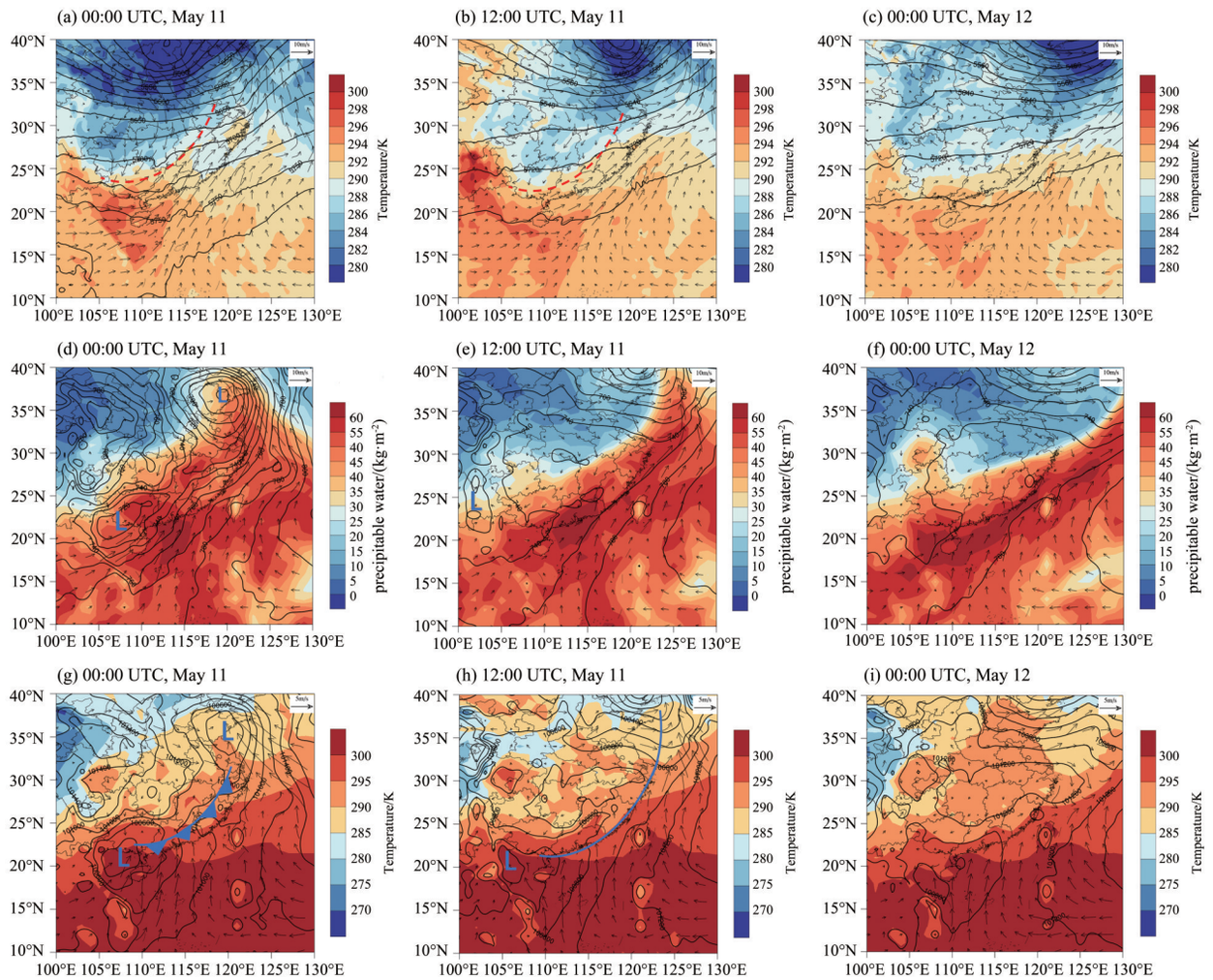

(a)-(c): The 500 hPa geopotential height (contour, unit: gpm) and the equivalent potential temperature at 850 hPa (shading, unit: K) superimposed with horizontal wind vector (arrows) at 850 hPa. (d)-(f): The 925 hPa geopotential height (contour, unit: gpm) and precipitable water (shading, unit: kg/m^2) superimposed with horizontal wind vector (arrows) at 925 hPa. (g)-(i): Sea level pressure (contour, unit: hPa) and surface temperature (shading, unit: K) superimposed with horizontal surface wind vector (arrows). Red dashed lines indicate the wind shear line at 850 hPa; blue lines denote surface fronts, and blue "L" symbols denote low pressure centers.

Fig. 2　Synoptic analysis (NCEP FNL Operational Global Analysis data) at 00:00 UTC on May 11 (left column), 12:00 UTC on May 11 (middle column), and 00:00 UTC May 12 (right column) in 2014

(Fig.2g-i) shows that the surface low was located over southwestern China and a synoptic-scale cold front existed to the north of Guangdong. These major synoptic features are similar to those reported in previous studies on coexisting frontal and WSHR over SC (Chen et al., 2018; Han et al., 2021).

During the selected event, the strong southwesterly BL jet could have brought abundant SSA across SC, which would have influenced the precipitation process. To investigate the effects of SSA on WSHR, we selected 00:00 UTC on May 11 to 00:00 UTC on May 12, 2014 as our study period.

4 Results

4.1 Effect of SSA on CCN

As described in Section 1, SSA can serve as CCN and participate in the formation of cloud droplets, thus affecting hydrometeor distribution, cloud lifetime, and precipitation. Vertical profiles of spatio-temporally averaged concentrations of SSA, PM_{10}, CCN (at supersaturation of 0.02%) over the key region from the three experiments are shown in Fig. 3.

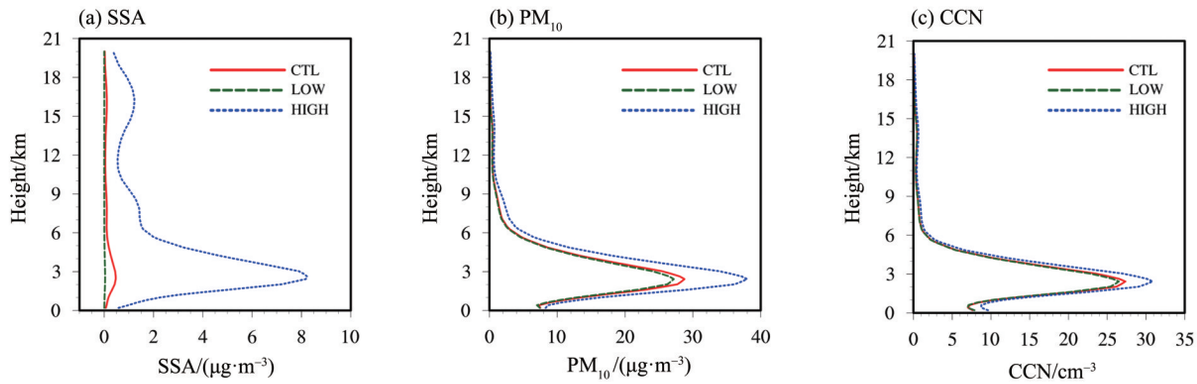

Fig. 3 Vertical profiles of spatiotemporally averaged concentrations of (a) sea salt aerosols (SSA), (b) PM_{10}, (c) cloud condensation nuclei (CCN, at supersaturation of 0. 02%) over the key region during 00:00 UTC on May 11 to 00:00 UTC on May 12, 2014 in experiments LOW (green dashed lines), CTL (red solid lines), HIGH (blue dashed lines)

Here, the supersaturation ratio is defined in the model as $S = \left(Q_v/Q_{sw} - 1\right) \times 100\%$, where Q_v is the mixing ratio of water vapor and Q_{sw} is the mixing ratio at water saturation. It can be seen that SSA, PM_{10} and CCN are primarily distributed below 9 km. The concentrations of SSA, PM_{10} and CCN are all first increases with height, reaching the maximum values at 3 km, then decreases with height. HIGH experiment has the largest concentrations of SSA, PM_{10} and CCN, followed by CTL experiment, the concentrations in LOW experiment are the smallest. This discrepancy is evident around 3 km. However, the difference in the number concentrations of SSA, PM_{10} and CCN is not of the same magnitude as that of SSA emission among three experiments, the trends of that three variables of LOW and CTL experiment are similar, while the trends between HIGH experiment and CTL are quite different. This phenomenon partly because of the scavenging mechanism of SSA. During the development of rainfall, strong turbulence and inertial action make SSA fall, causing them to be collected by falling hydrometeors. Moreover, the aerosols were subject to dry and wet deposition before they were activated as CCN in the fully online WRF-Chem model. Chameides et al. (1992) highlighted that SSA can remove sulfate particles in the atmosphere and inhibit CCN, indicating that the larger flux of SSA emissions causes a stronger removal process of sulfate particles in cloud. Therefore, it is reasonable that activation in the HIGH experiment is inhibited, causing a smaller increase in intensity of CCN in comparison with the CTL experiment.

4.2 Effect of SSA on precipitation

The observed and the simulated (CTL, LOW and HIGH experiments) 24 h accumulated precipitation are shown in Fig. 4. The CTL experiment reasonably reproduces the observed rainfall, even though positional bias exists, which is common in real-data simulations (Guo et al.,2022 ;Davis et al., 2009). The center of this rainfall is shifted northeastward in the CTL simulation relative to the observation, and the amount of simulated rainfall is higher than the rainfall amount in the CMORPH data. This discrepancy may be the result of two factors. First, the grid resolution of domain d03 is 4 km, while the CMORPH dataset provides grid-averaged precipitation at 0.1° resolution; therefore, the simulated precipitation is provided at higher resolution. Second, the Lin cloud scheme was used in this study. The Lin cloud scheme is a bulk scheme that uses a semi-empirical gamma or exponential size distribution to describe the cloud microphysical properties. Fan et al. (2012) highlighted that bulk schemes tend to produce higher cloud droplet numbers, which might result in overestimation of the rain mixing ratio and precipitation in numerical models.

Three experiments can reproduce the rainfall center, which is located in Shenzhen. The rain belt is distributed along the coastline. The precipitation in the LOW experiment is relatively dispersed, while that in the HIGH experiment is more concentrated. The 24 h averaged rainfall of the three simulations are 78.87 mm (LOW), 77.40 mm (CTL), and 77.19 mm

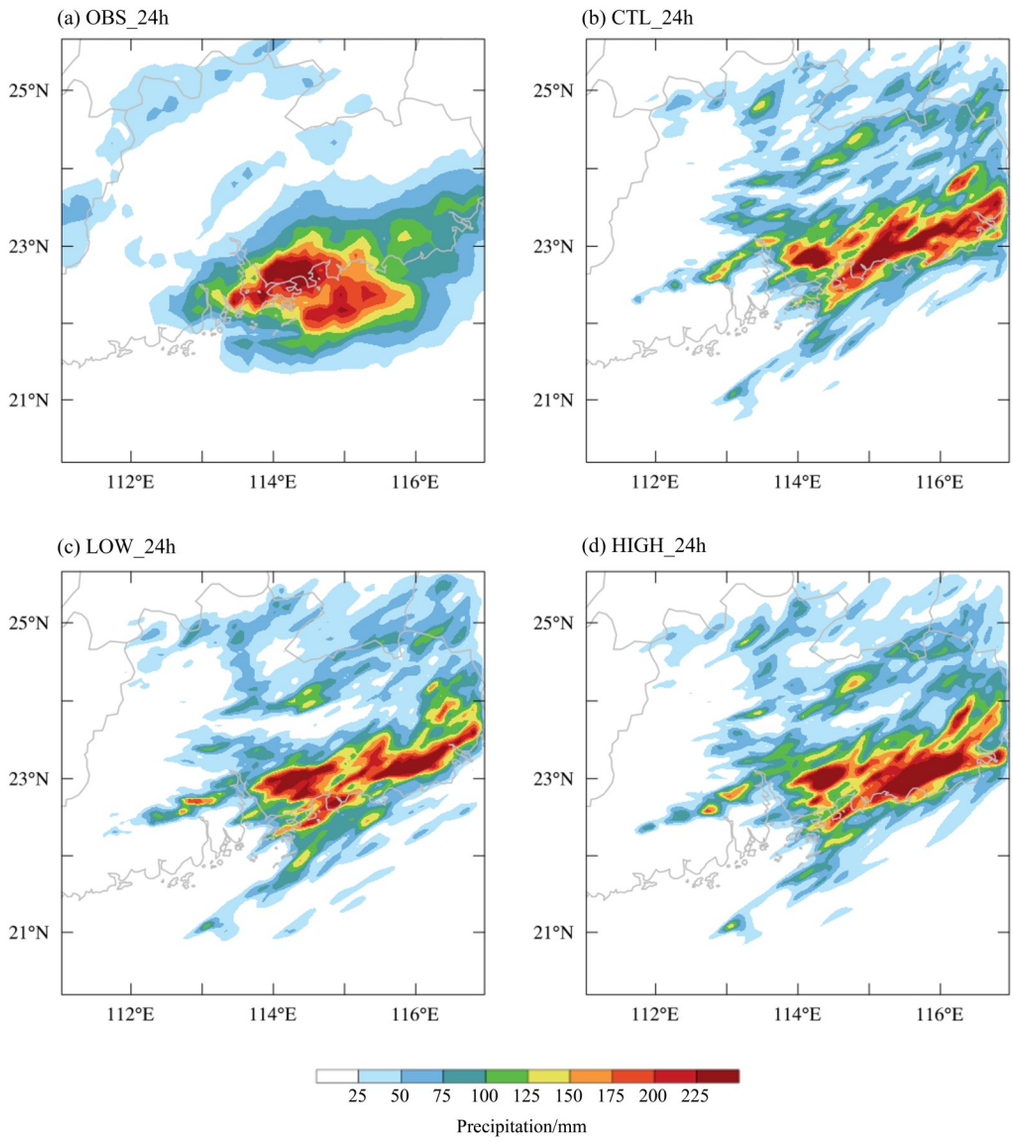

(a) observation data (OBS) and (b)-(d) simulation results from the CTL, LOW, and HIGH experiments, respectively. Gray lines denote coastlines and provincial boundaries. Observation precipitation data (0. 1° × 0. 1°) were provided by the Chinese National Meteorological Information Center (http://data. cma. cn/).

Fig. 4　The 24 h accumulated precipitation (shading, unit: mm) in domain d03 (Fig. 3b) during 00:00 UTC on May 11 to 00:00 UTC on May 12, 2014

(HIGH), respectively, while decreases by 2.18% under high sea salt aerosols emission. Therefore, accumulated precipitation decreases with increasing SSA. Although the differences in the values among the three simulations are small, it must be considered that the values are domain-averaged and that extreme rainfall usually happens locally.

The temporal variation in hourly precipitation over the key region in the observed data and the CTL simulation are compared in Fig. 5. It can be seen that the trend of hourly precipitation derived from the observation is consistent with that from CTL experiment during 00:00 UTC on May 11 to 00:00 UTC on May 12, 2014. CTL experiment well reproduces the peak rainfall rate during 01:00 to 02:00, when the observed and simulated rain rate is approximately 6 and 7 mm/h respectively. Observed rain rate shows a trough around 05: 00 while simulated trough appears at 06: 00. Experiment CTL fails to reproduce the peak value at 08: 00 in observation, which is about 1.5 mm less than observed precipitation and occurs at one hour later 09:00. During 12:00 on May 11 to 00:00 on May

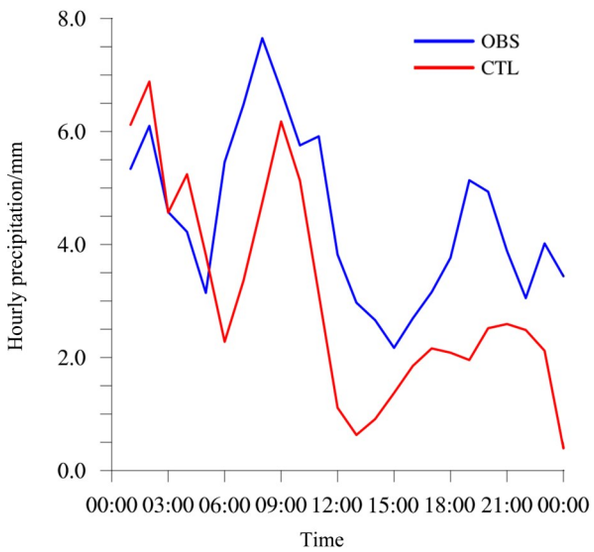

Observation precipitation data (0.1°×0.1°) were provided by the CNMIC (http://data.cma.cn/).

Fig. 5 Temporal variations in spatially averaged hourly precipitation (mm) over the key region (21. 5°−23. 5°N, 113°−115°E; black dashed rectangle in Fig. 1b) during 00:00 UTC, May 11 to 00:00 UTC, May 12, 2014

12, experiment CTL underestimates the rainfall, it may be the result of simulated precipitation area has shifted eastward (Fig. 4). The precipitation is out of the key region, therefore, the regional averaged precipitation in this period is underestimated.

To investigate the relationship between SSA and precipitation, the time averaged precipitation rates over the key region for three experiments are calculated. LOW experiment has the highest rain rate (3.15 mm/h), while the rain rate in CTL experiment and HIGH experiment is 3.10 and 3.09 mm/h,respectively. The averaged rain rate decreases with increasing SSA emission.

4.3 Effect of SSA on the distribution of hydrometeors

The influence of aerosols on precipitation cannot be clearly understood only by focusing on the surface precipitation and rain rate, analysis of hydrometeors is necessary. The vertical profiles of mixing ratio of different hydrometeors from the three experiments are presented in Fig.6. The mixing ratio of cloud droplets reaches the peak value of 0.10 g/kg at the height of 4 km, then decreases slowly with the increase of altitude, dropping to 0 at 11 km. The mixing ratio of rain water first increases with height and reaches the peak value of 0.38 g/kg around 4 km, then it slowly decreases with height, intersecting with the curve of graupel at 4.5 km and decreasing to 0 at 6 km. The values of ice and snow are relatively small, reaching the maxima at about 0.03 g/kg and 0.05 g/kg at 12 km and 11 km, respectively. The mixing ratio of graupel first increases and then decreases with height, reaching a peak of 0.4 g/kg at an altitude of about 6 km. Graupel melts into rain water at the height of 4.5 km. Among the five hydrometeors, graupel and rain water can fall to the ground to form precipitation.

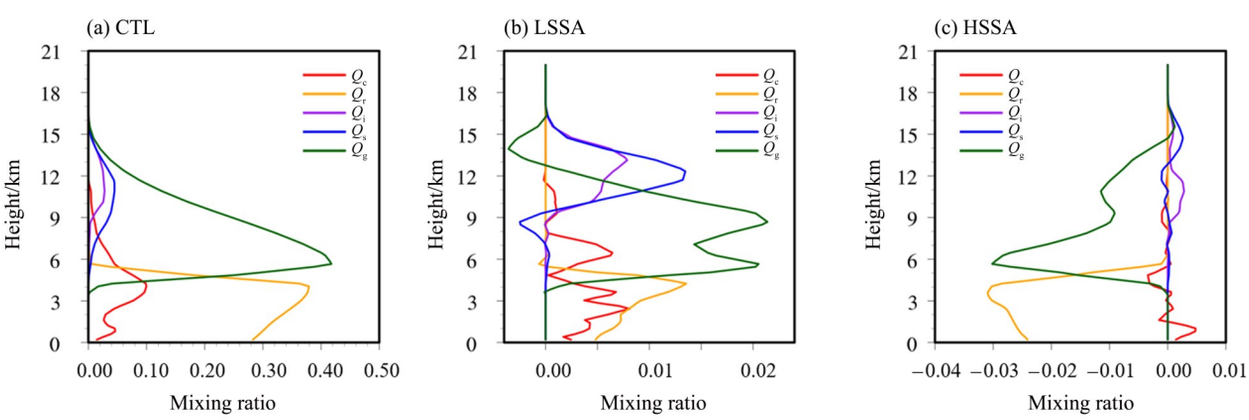

All results are averaged over the key region (21. 5°−23. 5°N, 113°−115°E; black dashed rectangle in Fig. 1b) during 00:00 UTC, May 11 to 00:00 UTC, May 12, 2014.

Fig. 6 Vertical profiles of mixing ratio of cloud droplets (Q_c, red lines), rain (Q_r, yellow lines), ice (Q_i, purple lines), snow (Q_s, blue lines), graupel (Q_g, green lines) (unit: g/kg) from (a) CTL, (b) LSSA: LOW minus CTL, and (c) HSSA: HIGH minus CTL

From the vertical profiles of the difference between the two sensitivity experiments and CTL (Fig. 6b, c), mixing ratio of five hydrometeors are larger in the LOW experiment than in the CTL, the mixing ratio of cloud droplets shows positive values at 0−11 km, the mixing ratio of rain water shows positive values at 0−6 km, and the difference between the LOW experiment and the CTL reaches a maximum value of 0.014 g/kg. The mixing ratio of ice and snow show positive values in the height range of 9−15 km, and the difference between the LOW experiment and the CTL reaches a maximum value of 0.008 at 13 km and 0.014 g/kg at 12 km, respectively. The mixing ratio of graupel shows positive value within 3−12 km, and the difference between the LOW experiment and the CTL reaches a maximum value of 0.022 g/kg at 9 km. Mixing ratio of rain and graupel are smaller in the HIGH experiment than in the CTL, they show negative values at 0−6 km and 3−15 km, respectively, while the mixing ratio of other hydrometeors show small changes. Table 1 gives the mixing ratio of five hydrometeors averaged over the key region, results of three experiments are also compared. In LOW experiment, the regional mixing ratio of five hydrometeors both larger than that in CTL. In HIGH experiment, the regional average amount decreased by 0.07 and 0.13 kg/m^2 relative to CTL, respectively, while the changes of other hydrometeors are smaller, which are consistent with the features shown in Fig. 6. Therefore, the mixing ratio of graupel and rain decrease with increasing SSA emission, indicating that SSA primarily affect the mixing ratio of graupel and rain to affect precipitation.

Table 1　Mixing ratio (Q_x, kg/m^2) of hydrometeors averaged over the key region during 00:00 UTC, May 11 to 00:00 UTC, May 12, 2014, from LOW, CTL and HIGH experiments, respectively[1)]

Variable	LOW	CTL	HIGH	LSSA	HSSA
Q_c	0.36	0.33	0.33	0.03 (7.54%)	0.00 (0.56%)
Q_r	1.59	1.55	1.42	0.04 (2.48%)	−0.13 (−9.28%)
Q_i	0.05	0.04	0.04	0.01 (20.17%)	0.00 (8.45%)
Q_s	0.10	0.09	0.10	0.01 (12.53%)	0.00 (1.52%)
Q_g	1.09	1.04	0.97	0.06 (5.37%)	−0.07 (−7.14%)

1) The subscripts c, r, i, s, g represent cloud droplets, raindrop, ice, snow, graupel in order. Columns LSSA and HSSA represent the results of LOW and HIGH minus CTL, respectively, with the values inside parentheses indicating the fractional difference relative to LOW or HIGH.

4.4 Effect of SSA on the latent heating of microphysical processes

The conversion parameter and release of latent heat during various cloud microphysical processes are important aspects in the development of rainfall. In this study, the conversion parameter and latent heat released through phase transitions (i. e., condensation, evaporation, deposition, sublimation, freezing, and melting) in each process were calculated using the following equations:

$$[P_x] = \sum_{i,j,k} p_x(i,j,k) \times \rho(i,j,k) \times \Delta z(k), \quad (2)$$

$$Q_{\text{proc}} = \frac{L P}{C}, \quad (3)$$

where P_x (kg·m^{-2}·h^{-1}) is the vertical integral of a specific microphysical process x, which is explained in detail in Table 2; p_x is the microphysical conversion rate on each grid (kg·kg^{-1}·h^{-1}), ρ is air density (kg/m^3), and $\Delta z(k)$ is the height difference between adjacent layers in the vertical direction (m). Meanwhile, Q_{proc} (K/h) represents the heating rate released or absorbed through phase transition, P (kg·kg^{-1}·h^{-1}) is the transition rate of a cloud microphysical process, L (J/kg) is the latent heat of condensation, freezing, and deposition per unit mass, and C (J·kg^{-1}·K^{-1}) is the specific heat of moist air at constant pressure.

Table 2 presents the results of the vertical integration using Eq. (2) of the 33 microphysical conversions averaged during 00:00 UTC May 11 to 00:00 UTC May 12, 2014 over the key region for all three experiments. Positive values represent an exothermic

Table 2 Vertical integration conversion rate of cloud microphysical processes（unit：kg·m^{-2}·h^{-1}）averaged during 00:00 UTC，May 11 to 00：00 UTC，May 12，2014 over the key region（21. 5°−23. 5°N，113°−115°E；black dashed rectangle in Fig. 1b）

Microphysical conversions	Description	LOW	CTL	HIGH	Trend
GACR	Graupel absorbs rain	36. 4	30. 9	28. 7	↓
COND	Water vapor condenses into cloud water	10. 0	9. 6	8. 4	↓
RAUT	Cloud water automatically converts to rain	3. 3	3. 1	2. 6	↓
RACW	Rainwater absorbs cloud water	2. 8	2. 7	2. 4	↓
SACR	Snow absorbs rain	2. 7	2. 4	2. 1	↓
GACW	Graupel absorbs cloud water	2. 3	2. 1	1. 9	↓
IACR	Cloud ice absorbs rain	1. 7	1. 5	1. 3	↓
GACS	Graupel absorbs snow	1. 3	1. 2	1. 3	↓/↑
IDEP	Cloud ice deposition	1. 1	1. 0	1. 0	—
SFI	Snow freezes cloud ice	1. 0	0. 9	0. 9	↓
GDEP	Graupel deposition	0. 7	0. 7	0. 6	↓
RACS	Rain absorbs snow	0. 1	0. 1	0. 1	—
SDEP	Snow deposition	0. 1	0. 1	0. 1	—
SACI	Snow absorbs cloud ice	0. 1	0. 0	0. 1	↓/↑
SACW	Snow absorbs cloud water	0. 1	0. 1	0. 1	—
IHOM	Cloud water homogeneously freezes into cloud ice	0. 1	0. 1	0. 0	↓
SSUB	Snow sublimation	− 0. 1	0. 0	0. 0	↓
ISUB	Cloud ice sublimation	− 0. 1	− 0. 1	0. 0	↓
GMLTEVP	Evaporation of melted graupel	− 0. 1	− 0. 1	− 0. 1	—
GSUB	Graupel sublimation	− 0. 2	− 0. 2	− 0. 2	—
CEVP	Cloud water evaporates into vapor	− 0. 8	− 0. 8	− 0. 7	↓
GMLT	Graupel melts into rain	− 6. 0	− 5. 3	− 5. 2	↓

process and negative values represent an endothermic process. In the simulated rainfall, the rain water collected by graupel (GACR) process has the greatest magnitude. The rates at which water vapor condenses into cloud water (COND), graupel melts into rain (GMLT), cloud water automatically converts to rain (RAUT), rainwater absorbs cloud water (RACW), snow absorbs rain (SACR) and graupel absorbs cloud water (GACW) are also larger than the other cloud microphysical conversion processes. Other microphysical conversions not shown are zero. Most of the cloud microphysical conversions decrease with increasing SSA concentration, except for the GACS process (graupel absorbs snow) and SACI process (snow absorbs cloud ice). In this case, larger SSA emission generates more CCN concentration (Fig. 3c), making competition between CCN enhanced under a limited water vapor condition, resulting in the cloud droplets decreased, which explain the decrease of the RAUT process (cloud water automatically converts to rain), RACW process (rainwater absorbs cloud water), and the reduce of precipitation in the HIGH experiment.

Aerosols can influence precipitation via dynamic and thermal processes. We analyzed the meridional vertical velocity of the three experiments. As shown in Fig. 7, the ascending motion from 113° to 114°E is weak, while the ascending motion from 114° to 115°E is relative strong. The ascending air from 114° to 115°E decreases with increasing SSA emission, which suppresses convection, decrease the mixing ratios of graupel and rain (Fig. 6). The vertical velocity is related to latent heat released during rainfall. Vertical profiles of latent heating rate in different phase-changing processes, total latent heating rate and the difference of that between two sensitivity experiments and CTL are presented in Fig. 8. In three experiments, the total la-

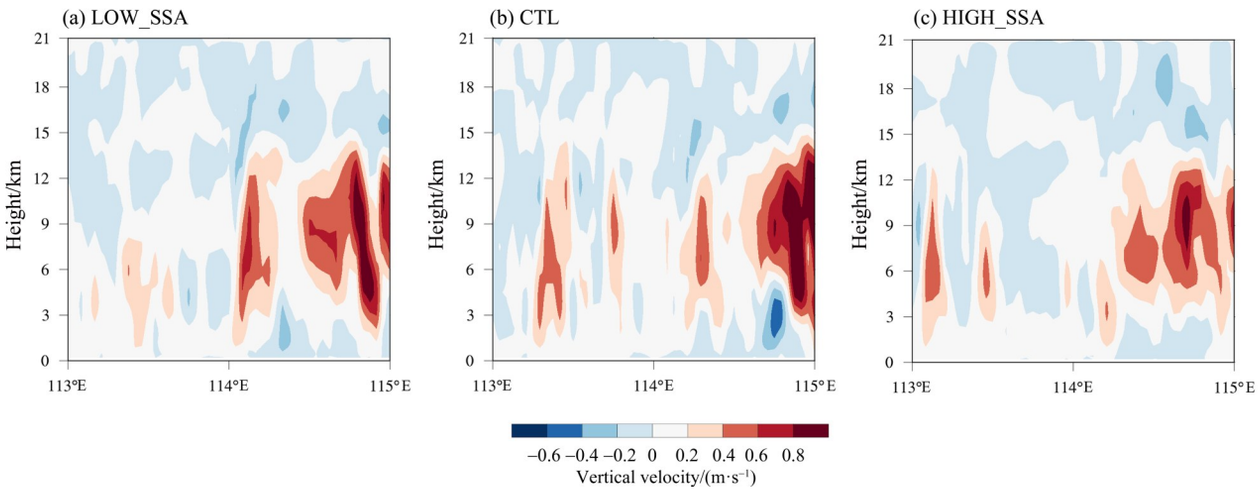

Fig. 7　Vertical profiles of vertical velocity (shading; unit: m/s) from the three experiments (a) LOW, (b) CTL, and (c) HIGH over the key region (21. 5°−23. 5°N, 113°−115°E; black dashed rectangle in Fig. 1b) during 00:00 UTC May 11 to 00:00 UTC May 12, 2014

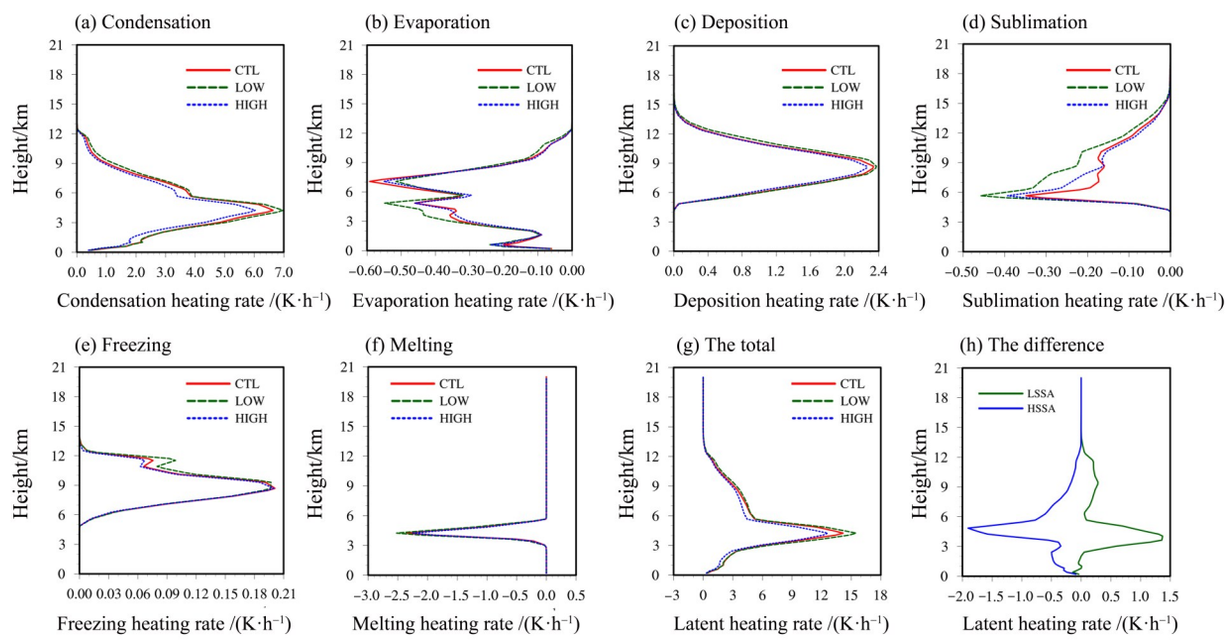

Fig. 8　Vertical profiles of the spatiotemporally averaged latent heating rate (K/h) due to different phase-changing processes: (a) condensation, (b) evaporation, (c) deposition, (d) sublimation, (e) freezing, (f) melting, and (g) total from the CTL (red solid lines), LOW (green dashed lines), and HIGH (blue dashed lines) experiments, and (h) the difference between two sensitivity experiments and CTL over the key region (21. 5°−23. 5°N, 113°−115°E; black dashed rectangle in Fig. 1b) during 00:00 UTC, May 11 to 00:00 UTC, May 12, 2014

tent heating rates increase from the ground, reaching peak values around 4 km, then decrease slowly with height. At the height of 6 km, the total latent heating rates start to decrease rapidly with height (Fig. 8g). Further analysis of the latent heat contributions indicates that peak values at 4 km depend mainly on the degree of latent heat from condensation, condensation heating rate dominates the total microphysics heating rate below 6 km. The accelerated rate of decrease in total latent heating rate with altitude at 6 km is mainly due to evaporation (Fig. 8b) and sublimation (Fig. 8d) processes. Comparing the three experiments, it can be seen that the total latent heating rate decreases with SSA emission (Fig.8h),the maximum difference reaches 1.5 K/h (LOW minus CTL),−1.8 K/h (HIGH minus CTL) at 4 km, respectively. Hence, an increase

of SSAs is beneficial to the suppression of the release of latent heat in a WSHR event.

5 Summary

This study used the WRF-Chem model version 4.1.2 with 3 nested domains to simulate a warm-sector heavy rainfall(WSHR) event that occurred over coastal Southern China. We investigated the impact of SSA on WSHR by conducting three experiments with different intensity of SSA emission, i. e., that of the LOW and HIGH experiments was 0.1 and 10 times that of the CTL experiment, respectively. The following conclusions were derived from analysis of the results of these three experiments.

1) SSA, PM_{10} and CCN are primarily distributed below 9 km. The concentrations of SSA, PM_{10} and CCN are all first increases with height, reaching the maximum values at 3 km, then decreases with height. HIGH experiment has the largest concentrations of SSA, PM_{10} and CCN.

2) SSA can affect rainfall area, the LOW experiment shows dispersed rainfall, whereas the rainfall in the HIGH experiment is more concentrated. The 24 h accumulated precipitation and averaged rain rate decreased with increasing SSA concentration.

3) Most of the cloud microphysical conversions decrease with increasing SSA concentration. High SSA concentrations provide higher numbers of CCN, leading to competition between CCN for the limited supply of water vapor, resulting in a decrease in cloud droplet size, which explain the decrease of the RAUT process (cloud water automatically converts to rain), RACW process (rain water absorbs cloud water), and the reduce of precipitation in the HIGH experiment.

4) Variations in latent heating rate have a direct influence on the thermodynamics of the WSHR. In the LOW experiment, a high latent heating rate leads to more latent heat released, resulting in an increase of the vertical velocity. In the HIGH experiment, less latent heat is released, weakening the updrafts, convection and decreasing precipitation.

This study used the Lin cloud scheme, which is an explicit bulk cloud model. The averaging of cloud particle size distribution over the spectrum in a bulk scheme decreases the response of hydrometeors in the bulk scheme to aerosols or CCN shape. Thus, a bulk scheme might produce a much higher cloud water mixing ratio. Moreover, very large SSAs can collect cloud water directly, but this process was not considered owing to limitations of the WRF-Chem model. These disadvantages regarding the bulk scheme could have affected the results regarding aerosol-cloud interaction in rainfall. An increase or decrease in the intensity of SSA emissions increase the amount of few cloud microphysical conversions, which is hard to explain to some extent due to many factors affecting the microphysical processes and hydrometeors, such as horizontal advection and vertical convection. The mechanism behind this is complex and nonlinear, which needs to further investigate. Because numerical simulations were performed for only one rainfall event in this study, these results will not necessarily be representative of all circumstances. Therefore, further simulations are necessary to broaden our understanding of WSHR.

References:

LEWIS R, SCHWARTZ E, 2004. Sea salt aerosol production: mechanisms, methods, measurements and models—A critical review[M]. Washington, D. C.: American Geophysical Union.

BARNARD J C, CHAPMAN E G, FAST J D, et al, 2004. An evaluation of the FAST-J photolysis algorithm for predicting nitrogen dioxide photolysis rates under clear and cloudy sky conditions[J]. Atmos Environ, 38(21): 3393-3403.

CHAMEIDES W L, STELSON A W, 1992. Aqueous-phase chemical processes in deliquescent sea-salt aerosols: A mechanism that couples the atmospheric cycles of S and sea salt[J]. J Geophys Res, 97(D18): 20565.

CHIN M, GINOUX P, KINNE S, et al, 2002. Tropospheric aerosol optical thickness from the GOCART model and comparisons with satellite and Sun photometer measurements[J]. J Atmos Sci, 59(3): 461-483.

DAVIS C A, GALARNEAU T J Jr, 2009. The vertical struc-

ture of mesoscale convective vortices[J]. J Atmos Sci, 66(3): 686−704.

DU Y, CHEN G, 2018. Heavy rainfall associated with double low−level jets over Southern China. part I: Ensemble−based analysis[J]. Mon Weather Rev, 146(11): 3827−3844.

FAN J, LEUNG L R, LI Z, et al, 2012. Aerosol impacts on clouds and precipitation in Eastern China: Results from Bin and bulk microphysics[J]. J Geophys Res, 117: D00K36.

GAO W H, ZHAO F S, HU Z J, et al, 2012. Improved CAMS cloud microphysics scheme and numerical experiment coupled with WRF model[J]. Chin J Geophys, 55(2): 396−405.

GONG S L, 2003. A parameterization of sea−salt aerosol source function for sub− and super−micron particles[J]. Global Biogeochem Cycles, 17(4): 1097.

GONG S L, BARRIE L A, PROSPERO J M, et al, 1997. Modeling sea−salt aerosols in the atmosphere: 2. Atmospheric concentrations and fluxes[J]. J Geophys Res, 102(D3): 3819−3830.

GRELL G A, DÉVÉNYI D, 2002. A generalized approach to parameterizing convection combining ensemble and data assimilation techniques[J]. Geophys Res Lett, 29(14): 1693.

GRELL G A, PECKHAM S E, SCHMITZ R, et al, 2005. Fully coupled "online" chemistry within the WRF model[J]. Atmos Environ, 39(37): 6957−6975.

GUENTHER A, KARL T, HARLEY P, et al, 2006. Estimates of global terrestrial isoprene emissions using MEGAN (Model of emissions of gases and aerosols from nature)[J]. Atmos Chem Phys, 6(11): 3181−3210.

GUO J, LUO Y, YANG J, et al, 2022. Effects of anthropogenic and sea salt aerosols on a heavy rainfall event during the early−summer rainy season over coastal Southern China[J]. Atmos Res, 265: 105923.

HAN B, DU Y, WU C, et al, 2021. Microphysical characteristics of the coexisting frontal and warm−sector heavy rainfall in South China[J]. JGR Atmospheres, 126(21): e2021JD035446.

HERBENER S R, van den HEEVER S C, CARRIÓ G G, et al, 2014. Aerosol indirect effects on idealized tropical cyclone dynamics[J]. J Atmos Sci, 71(6): 2040−2055.

IACONO M J, DELAMERE J S, MLAWER E J, et al, 2008. Radiative forcing by long−lived greenhouse gases: Calculations with the AER radiative transfer models[J]. J Geophys Res, 113(D13): D13103.

JIANG B, LIN W, LI F, et al, 2019. Sea−salt aerosol effects on the simulated microphysics and precipitation in a tropical cyclone[J]. J Meteorol Res, 33(1): 115−125.

JIMÉNEZ P A, DUDHIA J, GONZÁLEZ−ROUCO J F, et al, 2012. A revised scheme for the WRF surface layer formulation[J]. Mon Weather Rev, 140(3): 898−918.

LAMARQUE J F, EMMONS L K, HESS P G, et al, 2012. CAM−chem: Description and evaluation of interactive atmospheric chemistry in the Community Earth System Model[J]. Geosci Model Dev, 5(2): 369−411.

LI M, LUO Y, ZHANG D L, et al, 2021. Analysis of a record−breaking rainfall event associated with a monsoon coastal megacity of South China using multisource data[J]. IEEE Trans Geosci Remote Sens, 59(8): 6404−6414.

LIN Y L, FARLEY R D, ORVILLE H D, 1983. Bulk parameterization of the snow field in a cloud model[J]. J Climate Appl Meteor, 22(6): 1065−1092.

LIU Y, DAUM P H, 2004. Parameterization of the autoconversion Process. Part I: Analytical formulation of the kessler−type parameterizations[J]. J Atmos Sci, 61(13): 1539−1548.

LIVNEH B, RESTREPO P J, LETTENMAIER D P, 2011. Development of a unified land model for prediction of surface hydrology and land – atmosphere interactions[J]. J Hydrometeorol, 12(6): 1299−1320.

LOHMANN U, FEICHTER J, 2005. Global indirect aerosol effects: A review[J]. Atmos Chem Phys, 5(3): 715−737.

LUO H, JIANG B, LI F, et al, 2019. Simulation of the effects of sea−salt aerosols on the structure and precipitation of a developed tropical cyclone[J]. Atmos Res, 217: 120−127.

MONAHAN E C, SPIEL D E, DAVIDSON K L, A model of marine aerosol generation via whitecaps and wave disruption[M]// /MONAHAN E C, et al, eds. Oceanic Whitecaps: Oceanographic Sciences Library, Vol 2. Dordrecht: Springer, 1986: 167−174.

ROSENFELD D, 1999. TRMM observed first direct evidence of smoke from forest fires inhibiting rainfall[J]. Geophys Res Lett, 26(20): 3105−3108.

ROSENFELD D, 2000. Suppression of rain and snow by urban and industrial air pollution[J]. Science, 287(5459): 1793−1796.

ROSENFELD D, LAHAV R, KHAIN A, et al, 2002. The role of sea spray in cleansing air pollution over ocean via cloud processes[J]. Science, 297(5587): 1667−1670.

ROSENFELD D，LOHMANN U，RAGA G B，et al，2008. Flood or drought：How do aerosols affect precipitation?［J］. Science，321(5894)：1309−1313.

SKAMAROCK W C，KLEMP J B，2008. A time−split nonhydrostatic atmospheric model for weather research and forecasting applications［J］. J Comput Phys，227(7)：3465−3485.

TWOMEY S，1977. The influence of pollution on the shortwave albedo of clouds［J］. J Atmos Sci，34(7)：1149−1152.

WAN Q，WANG B，WONG W K，et al，2017. The Southern China monsoon rainfall experiment (SCMREX)［J］. Bull Am Meteorol Soc，98(5)：999−1013.

WIEDINMYER C，AKAGI S K，YOKELSON R J，et al，2011. The Fire INventory from NCAR (FINN)：A high resolution global model to estimate the emissions from open burning［J］. Geosci Model Dev，4(3)：625−641.

WILD O，ZHU X，PRATHER M J，2000. Fast−J：Accurate simulation of in− and below−cloud photolysis in tropospheric chemical models［J］. J Atmos Chem，37(3)：245−282.

WU N，ZHUANG X，MIN J，et al，2020. Practical and intrinsic predictability of a warm−sector torrential rainfall event in the South China monsoon region［J］. J Geophys Res Atmos，125(4)：e2019JD031313.

WU Z，CAI J，LIN L，et al，2018. Analysis of mesoscale systems and predictability of the torrential rain process in Guangzhou on 7 May 2017［J］.Meteorological Monthly，44(4)：485−499.

XIAO H，YIN Y，JIN L，et al，2014. Simulation of aerosol effects on orographic clouds and precipitation using WRF model with a detailed Bin microphysics scheme［J］. Atmos Sci Lett，15(2)：134−139.

ZAVERI R A，EASTER R C，FAST J D，et al，2008. Model for simulating aerosol interactions and chemistry (MOSAIC)［J］. J Geophys Res，113(D13)：D13204.

ZAVERI R A，PETERS L K，1999. A new lumped structure photochemical mechanism for large−scale applications［J］. J Geophys Res，104(D23)：30387−30415.

ZHANG Q，STREETS D G，CARMICHAEL G R，et al，2009. Asian emissions in 2006 for the *NASA* INTEX−B mission［J］. Atmos Chem Phys，9(14)：5131−5153.

海盐核对华南沿海一次暖区暴雨的影响

罗青[1,2]，陈子健[1,2]，林文实[1,2]，蒋宝林[3]，曹琪敏[1]，李芳洲[1]

1. 中山大学大气科学学院 / 广东省气候变化与自然灾害研究重点实验室，广东 珠海 519082
2. 南方海洋科学与工程广东省实验室(珠海)，广东 珠海 519082
3. 惠州学院地理与旅游学院，广东 惠州 516007

摘要： 采用中尺度数值天气模式WRF-Chem 4.1.2，模拟了2014年在华南沿海地区发生的一次暖区强降水事件。通过进行3个不同海盐核排放强度(CTL，LOW，HIGH)试验，从降水落区、水成物分布、微物理过程以及潜热释放方面，探讨了海盐气溶胶浓度对暖区暴雨的影响。研究结果表明，海盐核浓度对降水落区有一定的影响，低海盐核排放下的降水区域更分散，而高海盐核排放下的降水区域更集中。低(高)海盐核排放情况下，降水中的云凝结核浓度减少(增加)、雨水和霰的混合比增加(减少)、云微物理过程尤其是云水自动转化成雨水及云水被雨水收集过程增强(减弱)、潜热释放增加(减小)以及上升运动增强(减弱)，导致累计降水增多(减小)及降雨率增大(减小)。

关键词： 海盐核；暖区暴雨；微物理效应；WRF-Chem模式

（责任编辑　秦社彩）